Far-field dipole noise extracted from time-resolved PIV over separated aerofoils

D. W. Carter[1,*], B. Ganapathisubramani[1]
1: Dept. of Aeronautical and Astronautical Engineering, The University of Southampton, UK
* Correspondent author: D.W.Carter@soton.ac.uk

Keywords: PIV pressure estimation, aeroacoustics, separated aerofoils

ABSTRACT

We demonstrate far-field dipole acoustics from time-resolved planar particle image velocimetry (PIV) data for turbulent separated flow over NACA 0012 and NACA 65-410 aerofoils at a chord-based Reynolds number $Re_c \approx 7.1 \times 10^4$. The efficacy of the pressure reconstructions is demonstrated through a comparison with RANS simulations and surface pressure power spectra from the work of Zang *et al.* (2021). The pressure reconstructions are used in combination with Curle's analogy to determine the far-field noise generation. The noise directivity is found to be determined mostly by the geometry, with similar overall sound power level for both aerofoils. Through use of the data-driven spectral Linear Stochastic Estimation (sLSE) technique, the turbulent structures most correlated to the far-field noise are identified. In transient stall conditions, the location of correlated structures suggests shear layer flapping as the dominant mechanism. In deep stall, the correlated structures are concentrated further downstream in proximity to the trailing edge.

1. Introduction

Separation in aerofoils is a situation commonly encountered over a range of engineering applications such as the dynamic stall of a turbine blade encountering a sudden change in wind direction. The generation of noise in these flows is a subject of long-lasting interest due to the undesirably high noise levels and has motivated efforts to model such generation (Brooks *et al.* 1989) and determine the relevant mechanisms, such as using direct microphone measurements (Lacagnina *et al.* 2019, Zang *et al.* 2021) or through numerical simulation (Turner & Kim 2020). In the past decade, the use of time-resolved particle image velocimetry to determine pressure fields (Laskari *et al.* 2016; van Gent *et al.* 2017) and resulting far-field noise using acoustic analogies has been demonstrated in cavity flows (Koschatsky *et al.* 2011a,b). Despite this progress, there is a lack of experimental work dedicated to using time-resolved PIV specifically in the turbulent flow over separated, or *stalled*, aerofoils to determine far-field noise mechanisms.

The present work seeks to fill this knowledge gap by leveraging spatial information from time-resolved PIV fields with the temporal behavior of the far-field acoustics to ultimately

correlate instantaneous flow structures with noise mechanisms. In section 2 the experimental methodology and chosen parameter space will be introduced. The pressure reconstruction methodology and comparison to independently obtained results is presented in section 3. In section 4 the implementation of Curle's acoustic analogy to extract the far-field noise is described. In section 5 a data-driven framework to elucidate noise generation mechanisms in the velocity fields will be introduced. Finally, discussion and conclusions are drawn in section 6.

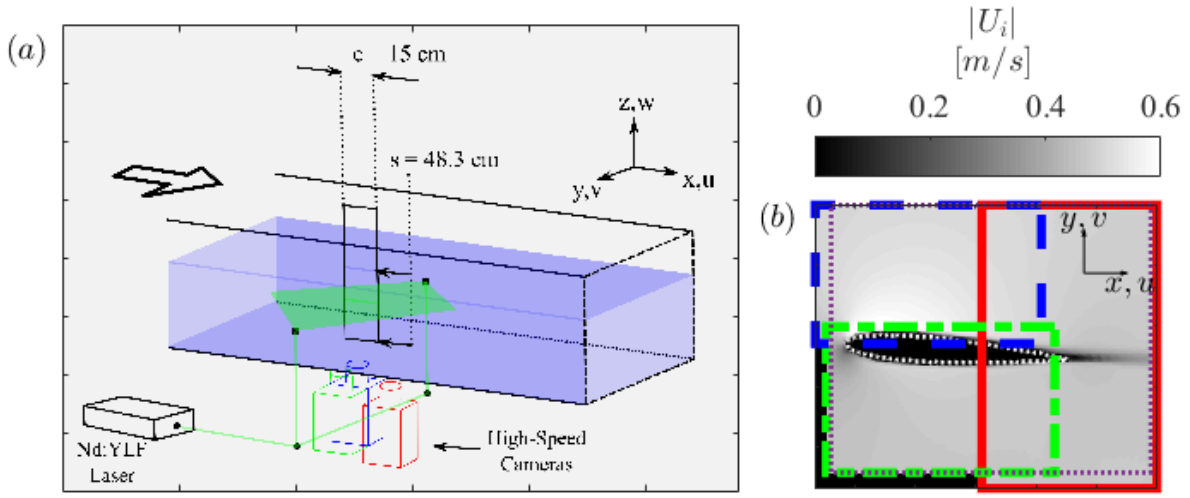

Fig 1: Diagram (not to scale) of the experimental setup in the water channel facility to perform high-speed PIV (a). The pseudo-color of velocity magnitude for the NACA 0012 at $\alpha = 4°$ is presented in (b) with the individual fields of view of the overlapping images indicated.

2. Experimental Data Sets

Time-resolved particle image velocimetry (PIV) data was collected in the University of Southampton water flume facility, featuring a test section 6.75 m long, a span of 1.2 m and water depth of 0.5 m. The aerofoil models of chord length $c = 15$ cm and span $s_{tot} = 70$ cm were fixed vertically in the center of the span of the flume immediately following the contraction into the test section. The portion of the span that was submerged was $s = 48.3$ cm. PIV imaging was performed in the stream-wise surface-normal (x-y) plane as illustrated in figure 1a. An overhead carriage system was employed to allow precise control of the angle of attack α. Angles of attack in the range $4° \leq \alpha \leq 17°$ at a chord-based Reynolds number $Re_c = \frac{U_\infty c}{\nu} \approx 7.1 \times 10^4$ (with U_∞ the free stream velocity, c the chord length, and ν the kinematic viscosity) were explored corresponding to a variety of stall conditions. An overview of the experimental cases is presented in table 1. A high-speed Nd:YLF laser (527 nm Litron) was directed inwards from either side of the facility to simultaneously illuminate the pressure, suction, and trailing regions of the aerofoil and three 4

megapixel (2560 x 1600 pixels) high-speed Phantom Veo 640-S cameras mounting 105 mm Ex Sigma lenses (f# 5.6) were synchronized to capture the flow field surrounding the plane of the aerofoil (figure 1b). Caution was exercised to ensure the laser sheets were aligned within the same plane, with an estimated sheet thickness of 2 mm at the location of the foil mid-chord. To compute the force quantities at each angle of attack, a six-axis force/torque load cell (ATI Delta IP65) was mounted to the aerofoil and synchronized to the PIV acquisition using an NI USB-6251 DAQ.

Table 1: Parameters of experimental cases.

Profile	α°	C_L
NACA 0012	4	0.30±0.1
NACA 0012	13	0.51±0.1
NACA 0012	15	0.49±0.1
NACA 65-410	13	0.68±0.1
NACA 65-410	15.5	0.64±0.2
NACA 65-410	17	0.65±0.1

The flow was seeded with Vestosint 2157 polyamide particles of nominal diameter 55 μm until a satisfactory seeding density was obtained. For each case simultaneous high-speed images were collected across cameras at a frequency of 1 kHz and stored until memory limitations were reached, resulting in 5.367 seconds of continuous data. Five runs were repeated resulting in 26.84 seconds of data for each case, corresponding to approximately 90 eddy turnover times $T_L = c/U_\infty$. The raw images of each camera were individually processed with background subtraction and Gaussian high-pass filtering with a filter width of 10 pixels to isolate the high-frequency particle reflections. Multi-pass planar PIV was performed using a verified in-house Matlab code with 3 passes per window size and square windows decreasing from 64 by 64 pixels, to 32 by 32 pixels, to 24 by 24 pixels with 50% overlap. The final vector spacing was Δx=0.83 mm corresponding to 181 vectors spanning the airfoil chord. PIV outliers were replaced using robust principle component analysis (Scherl *et al.* 2020) with the sparsity parameter at the theoretical optimum of $\lambda_s = 1$ and the inexact augmented Lagrangian method for iteration (Lin *et al.* 2010; Sobral *et. al.* 2016).

Prior to each measurement case, a calibration image spanning all three cameras was collected using a target aligned with the laser sheet plane. This was used to correct distortions and calibrate the PIV fields. The overlap across the fields of view within the calibration images was used for reference positions to stitch the velocity fields together (Raffel *et al.* 2018). The stitching was performed on the calibrated vector fields using a hamming window for blending. To account

for the unequal PIV grid sizes, the PIV vectors of the highest resolution grids (the suction and pressure fields of view) were bi-linearly interpolated to the lowest resolution grid (the trailing field of view) to avoid spatial up-sampling during stitching. Due to the airfoil extending downwards in the direction of the upward-facing cameras, a visual occlusion was produced on the pressure side of the aerofoil, preventing from measuring the flow close to the surface. In addition to the foil cross section, the occluded region was masked in the final vector fields. Surface profiles on the pressure side reported hereafter are linearly interpolated to the location of the foil surface using the nearest available data points. The final PIV fields were spatially truncated along the edges to form a rectangular domain (figure 1b).

Upon inspection of the time-resolved data, several anomalous high-frequency spectral peaks were observed in both the forces and velocity fields, starting at 15 Hz with a secondary harmonic peak at 30 Hz. It was determined that such a peak was likely due to a mechanical vibration within the overhead carriage system used to mount the airfoil. To avoid this artifact, all forces and velocity fields were temporally filtered to 10 Hz using a Gaussian low-pass filter. This limits the scope of the temporal analysis of the present work to frequencies below a non-dimensional frequency $f^\star = \frac{fc}{U_\infty} \leq 3$.

3. Instantaneous Pressure Reconstruction

To extract the far-field acoustics, it is first necessary to determine the instantaneous pressure. Planar pressure fields were reconstructed from the instantaneous velocity fields using a Poisson solver approach (de Kat & Van Oudheusden 2012; Laskari *et al.* 2016) for which the divergence of Navier-Stokes momentum equations is invoked:

$$\nabla^2 p = -\rho \nabla \cdot \left(\frac{\partial \boldsymbol{u}}{\partial t} + \boldsymbol{u} \cdot \boldsymbol{\nabla u} - \nu \nabla^2 \boldsymbol{u} \right) \quad (1)$$

where p is the instantaneous pressure field, ρ is the (constant) density, and u_i is the instantaneous velocity vector fields. Neumann boundary conditions were applied on the inlet and outlet boundaries of the domain and Dirichlet boundary conditions were employed using Bernoulli's equation in the free stream on both the suction (upper) and pressure (lower) domain boundaries. Due to the presence of reverse flow in the separated region, Taylor's hypothesis was not invoked to estimate the unsteady velocity term $\partial u_i / \partial t$ (Laskari *et al.* 2016). Instead, the unsteady velocity term was directly computed from the highly time-resolved Eulerian fields (Jakobsen *et al.* 1997). Good agreement using central temporal differences up to sixth order was found, therefore second order gradients were opted for in favor of processing speed. Spatial derivatives were computed using second-order central differences.

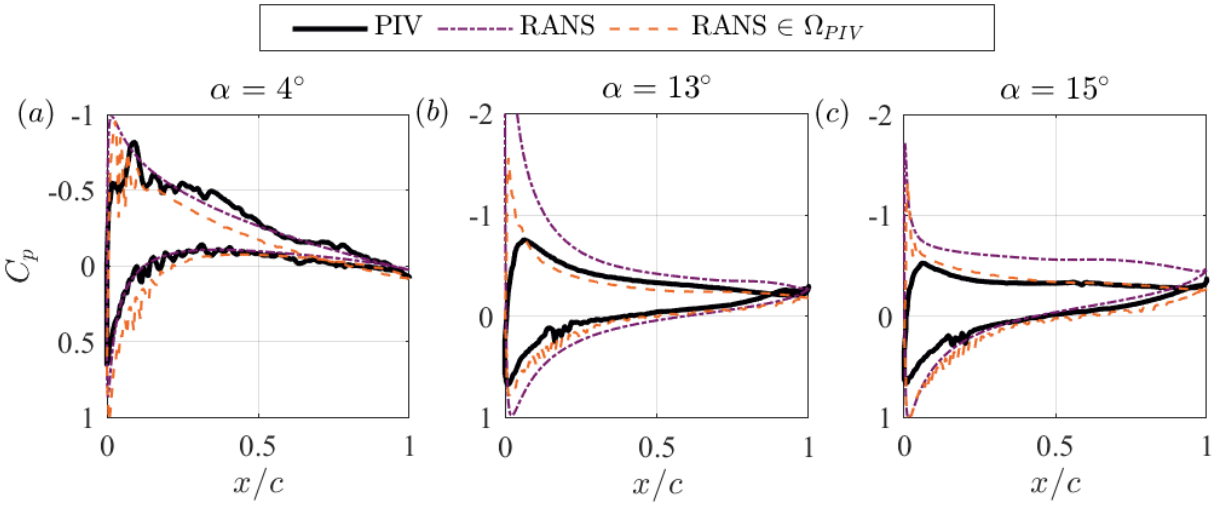

Fig 2: Mean surface pressure coefficient for the NACA 0012 cases from the PIV (solid) compared to a full-domain RANS simulation (dash dot) and the RANS data interpolated to the PIV grid domain and solved for using the Poisson solver (dashed).

To provide comparison for the mean pressure fields computed from planar PIV, an unsteady two-dimensional Reynolds-averaged Navier-Stokes (RANS) simulation was performed for the NACA 0012 cases using OpenFOAM software. The simulation utilized a k-ω shear stress transport (SST) closure model. A standard C-type domain and grid geometry was chosen with a horizontal and vertical extent of 20 chords lengths. The simulation properties (e.g. kinematic viscosity, inlet velocity, chord length) were chosen to match identically those of the experiment. The comparison between the surface pressure coefficient $C_p = P/\frac{1}{2}\rho U_\infty^2$ (with P the mean pressure and ρ the density) in the PIV and RANS is shown in figure 2. The agreement in the attached case (figure 2a) is found to be satisfactory, except for the leading edge (LE) where the PIV underestimated the suction peak. At higher angles of attack (figure 2b,c), despite good qualitative agreement, the PIV was found to significantly under-predict the magnitude of the surface pressure on the suction side. As the pressure at each point is the result of an integral spanning all points in the domain, the degree to which the field of view and PIV grid spacing impacts the pressure reconstruction must be taken into consideration. To assess the extent to which the domain size impacts the pressure reconstruction, the RANS velocity fields were interpolated to a grid and domain Ω_{PIV} matching that of the PIV cases and the pressure was reconstructed using the Poisson solver. The resulting surface pressures are also plotted in figure 2 and clearly indicate that the under-estimation in the surface pressure on the suction side is mostly attributed to the restricted PIV domain size.

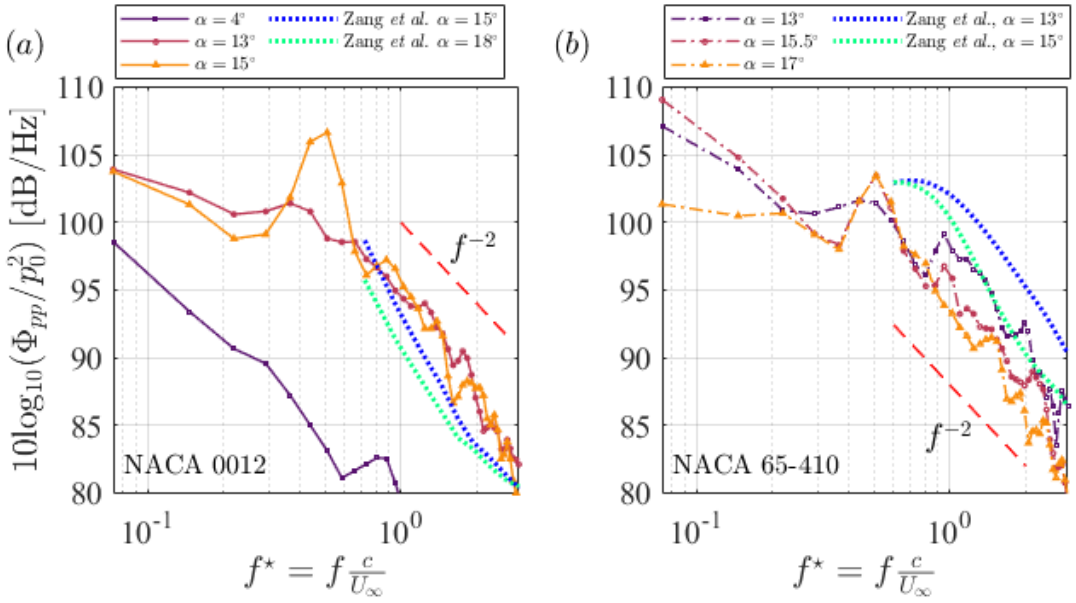

Fig 3: Pressure spectra from PIV on the surface of the aerofoils at $x/c = 0.9$ for the NACA 0012 cases (left) and NACA 65-410 cases (right). A water-to-air scaling was applied to allow for direct comparison to the surface pressure measurements of Zang *et al.* (2021) at moderately higher Reynolds number. Note here the reference pressure $p_{ref} = 20\ \mu Pa$.

Naturally, it is important to investigate whether and how the underestimated mean pressure on the suction side impacts the time-varying behavior. To do this, the instantaneous pressure reconstructions were assessed through inspection of the power spectral density taken at a point on the surface near the trailing edge (TE) at $x/c = 0.9$ as presented in figure 3. For this figure, the pressure magnitude was re-scaled using the equivalent freestream velocity at the same Reynolds number in air to define an equivalent dynamic pressure in air. Assuming the pressure fluctuations scale with the dynamic pressure, this rescaling allows for an approximate comparison to the wind tunnel surface microphone measurements of Zang *et al.* (2021), who investigated the same aerofoil geometries at a moderately higher Reynolds number of $Re_c = 4.2 \times 10^5$. Excellent agreement is found in the magnitude of the surface pressure in the separated cases on the order of 100 dB at the lowest frequencies. A power-law decrease in the separated cases of f^{-2} is also observed. In contrast to Zang *et al.* (2021), a local frequency peak in the separated cases near $f^\star = 0.4$ is observed, likely due to a coherent leading-edge vortex shedding that is more pronounced for the lower Reynolds number in the present data. Despite this difference, the power-law agreement in the spectral content and the average surface pressure distributions with the domain-restricted RANS simulations indicate satisfactory pressure reconstructions from PIV in the present study.

4. Acoustic Extraction via Curle's Analogy

The far-field acoustics surrounding the aerofoil physically belongs to a domain much too large to measure directly via experiment. Therefore, Curle's acoustic analogy is adopted (Curle 1955) utilizing the pressure fluctuations obtained from the PIV to estimate the far-field noise. Following the work of Larsson *et al.* (2004), the original solution presented by Curle is modified and the dipole sources emanating from the surface of the aerofoil are isolated in the surface integral (see also Koschatzky *et al.* 2011):

$$p_a(\boldsymbol{x},t) - p_{a,0} = \frac{1}{4\pi}\int_S l_i n_j \left(\frac{\dot{p}\delta_{ij}}{a_0 r}\right)\Big|_{\left(t-\frac{r}{a_0}\right)} dS(\boldsymbol{y}) \qquad (2)$$

where p_a is the acoustic pressure and $p_{a,0}$ the steady far-field pressure, l_i is the listener unit vector pointing from the source to the listener position, n_j is the surface normal unit vector, $\dot{p} = \partial p/\partial t$ is the unsteady pressure, a_o is the speed of sound, $r = |y_i - x_i|$ is the distance to the listener position x_i form the source y_i, and the surface S is the aerofoil surface. The integrand is evaluated at the retarded time $t - r/a_0$. Larsson *et al.* (2004) identified the dipole sources of equation 2 as the dominating sources of far-field noise for an open cavity flow (as opposed to the volume integral of Curle's solution involving quadrupole sources). This is consistent with the source intensity scaling predicted by Curle (1955). For stalled aerofoils, previous work suggests the dipole sources are likewise dominant (Moreau *et al.* 2009; Laratro *et al.* 2014). A similar analysis as the present study was presented using numerical simulations by Turner & Kim (2020) at Mach 0.4. Following their analysis, we adopt listener positions in a semi-circular array at a radius of ten chord lengths from the aerofoil mid-chord position for $0° \leq \theta \leq 180°$ spanning the suction side of the aerofoil at $N = 30$ locations. Here, $\theta = 0°$ is defined with respect to the LE at each angle of attack (not with respect to the direction of free stream velocity).

To perform the integral, surface normal vectors were defined at each PIV vector location along the mask of the aerofoils for all cases considered. A Savitsky-Golay filter was employed for smoothly varying surface normal estimates. This was found to be necessary particularly near the LE with significant curvature. The unsteady pressure $\dot{p}$ along the surface of the aerofoils was obtained directly through finite second-order temporal differences of the pressure. To reduce noise, a sliding average was used to smooth the unsteady pressure estimates with a width of 25 ms, corresponding to a non-dimensional frequency $f^\star = 12$. This does not impact the acoustic frequencies of interest in the present study that are restricted to $f^\star \leq 3$.

In general, the far-field approximation restricts the range of acoustic wavelengths λ to those that satisfy $\lambda \ll r$. This condition constrains the range of temporal frequencies to those that satisfy the far-field assumption as $f \gg a_0/r$. This is problematic for the present data set for which $r = 10c = 1.5$ m so that $a_0/r = 987$ Hz but the range of resolved frequencies in the spectra is $0.25 \leq f \leq 10$ Hz.

There are several considerations to be made regarding this issue. For example, one might instead adopt a listener distance r that satisfies the far-field constraint given the range of frequencies. In the present study this corresponds to a minimum distance of $r \approx 40{,}000c$. At this distance, the retarded time offset is so large that the spectrum of the acoustic pressure lies outside the frequencies of interest. It is important to note, however, that the frequency content of the acoustic spectrum via equation (3) remains the same regardless of r. Only the magnitude and time delay are impacted by the listener distance. It is therefore equally instructive to maintain a listener distance of $r = 10\ c$ and investigate the full spectrum of acoustic fluctuations originating from the unsteady source term $\dot{p}/a_0 r$. The important caveat being that, in the far-field, the magnitude of the acoustic pressure will decrease linearly with distance from the source.

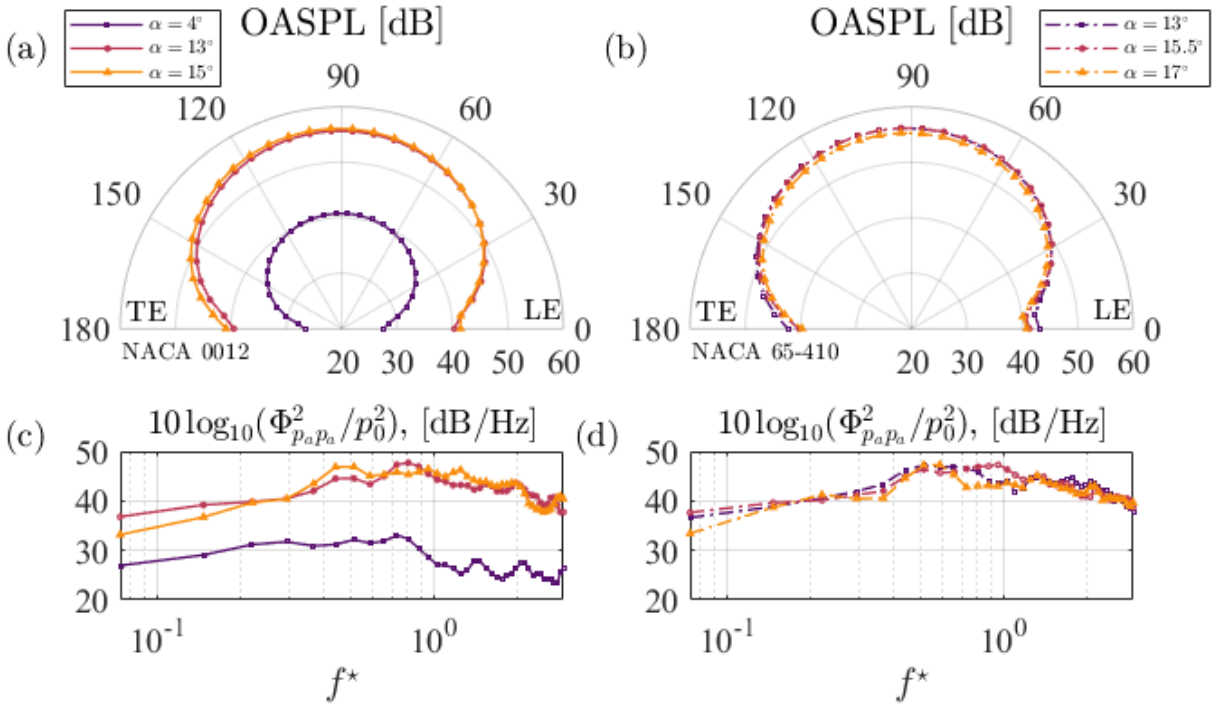

Fig 4: Acoustic directivity plots (a,b) for listener positions between $0° \leq \theta \leq 180°$ and pre-multiplied orientation-averaged sound power level spectra (c,d) at $r = 10c$ for the NACA 0012 cases (a,c) and NACA 65-410 cases (b,d) obtained using equation (3). Note here the reference pressure $p_0 = 1\ \mu Pa$.

The far-field acoustics estimated via equation 2 are shown in figure 4 for all cases. The overall sound power level (OASPL) directivity indicates the direction of sound is large geometry-driven, with maximum power at $\theta = 90°$ (normal to the foil chords). No significant differences in the shape of the distributions were found after considering band-limited directivity. For the stalled cases, the directivities are slightly asymmetric with approximately 2dB more sound power for $\theta > 120°$ (in proximity to the TE) with respect to $\theta < 60°$ (in proximity to the LE). The noise is generally comparable across stalled cases. The spectra in (c,d) indicate a broad band distribution reminiscent of jet noise, with no clear peak frequencies. The shape of the distributions agrees reasonably well with the far-field noise spectra of Mayer *et al.* (2020) for their data of a NACA 0012 aerofoil at $\alpha = 12°$ and $Re_c = 4.2 \times 10^5$. The comparatively low frequencies of the present study capture the hump of the distributions near $f^* \approx 0.5$.

A remaining challenge is to identify the flow structures that are responsible for the generation of far-field noise. For this reason, a data-driven approach is applied in the following section to the acoustic reconstruction of the stalled cases.

5. Noise sources via spectral linear stochastic estimation (sLSE)

To elucidate flow structures responsible for the dipole noise generation, the spectral Linear Stochastic Estimation (sLSE) is leveraged between the instantaneous velocity fields and the far-field acoustics pressure (Tinney *et al.* 2006). Specifically, the sLSE is performed between the acoustic pressure fluctuations at each listener location and the coefficients of the modes of the velocity fields via the proper orthogonal decomposition (POD; Sirovich 1987). In the following we present a brief outline on the application of this technique for the present analysis. The reader is referred to, e.g. Taira *et al.* (2017) and Podvin *et al.* (2018) for more details on POD and combining POD with LSE respectively.

The POD decomposes the velocity fluctuations u_i' as

$$u_i'(\boldsymbol{x}, t) = \sum_{k=1}^{K_{tot}} a_k(t)\phi_k(\boldsymbol{x}) \qquad (3)$$

where k is the mode number, K_{tot} is the total number of modes, $a_k(t)$ is the k-th instantaneous POD coefficient, and ϕ_k the k-th orthogonal spatial mode. For the present study a total of $K_{tot} = 1075$ modes are used to generate the POD basis and up to $K = 30$ modes are retained. The results were not found to change beyond 30 modes. In the present context, the sLSE leverages the temporal cross-correlation between the mode coefficients and the acoustic pressure fluctuations to

obtain the portion of the velocity fields most correlated to the noise. To perform this, two matrices are defined as

$$W_{ij} = \begin{bmatrix} \langle p_{a,1} p_{a,1} \rangle & \cdots & \langle p_{a,N} p_{a,1} \rangle \\ \vdots & \ddots & \vdots \\ \langle p_{a,1} p_{a,N} \rangle & \cdots & \langle p_{a,N} p_{a,N} \rangle \end{bmatrix} \qquad (4)$$

$$V_{ij} = \begin{bmatrix} \langle a_1 p_{a,1} \rangle & \cdots & \langle a_K p_{a,1} \rangle \\ \vdots & \ddots & \vdots \\ \langle a_1 p_{a,N} \rangle & \cdots & \langle a_K p_{a,N} \rangle \end{bmatrix} \qquad (5)$$

where the angled brackets $\langle \circ \rangle$ denote ensemble averaging and N is the total number of listener positions. These two matrices are used to obtain the spectral LSE coefficients as

$$B_{kj}(f) = W_{jk}(f)^{-1} V_{ji}(f) \qquad (6)$$

where $W_{jk}(f) = \{W_{jk}(\tau)\}$ and $V_{ji}(f) = \{V_{ji}(\tau)\}$ are the Fourier transforms of equations 4 and 5 where the dependence on the frequency f implies the Fourier domain. In practice the sLSE coefficients are obtained for each run individually and ensemble averaged for each case. Once the sLSE coefficients are obtained, the estimated POD coefficients are calculated in each run as

$$\tilde{A}_{ki} = \{B_{kj}(f) P_{a,ji}(f)\}^* \qquad (7)$$

where $P_{a,ji}(f)$ is the Fourier transform of the matrix of acoustic pressure fluctuations of size $[N \times n_t]$ where n_t is the number of times steps in the run, $\{\circ\}^*$ denotes the inverse Fourier transform, and $\tilde{A}_{ki}$ is the matrix of estimated POD coefficients of size $[K \times n_t]$. The velocity fields correlated with the noise are then reconstructed via

$$\tilde{u}_i'(\boldsymbol{x}, t) = \sum_{k=1}^{K} \tilde{a}_k(t) \phi_k(\boldsymbol{x}) \qquad (8)$$

where $\tilde{a}_k(t)$ is the k-th mode coefficient and time instant of the matrix $\tilde{A}_{ki}$. The main advantage of performing the LSE in the Fourier domain is the automatic incorporation of time delays in the estimation of the LSE coefficients (Tinney *et al.* 2006).

To highlight the spatial organization of the structures correlated to the far-field noise, the planar turbulent kinetic energy (TKE), defined as $k = 0.5(\langle u'^2 \rangle + \langle v'^2 \rangle)$, is computed for the

original fields and for the correlated fields. The contours highlighting the regions of concentrated TKE for both quantities are shown in figure 5. The velocity fields tend to have concentrated TKE at the incipient shear layer originating at the LE as well as the shear layer at the TE. In contrast, the correlated TKE is concentrated closer to the trailing edge at the height of the shear layer. For $\alpha = 13°$, corresponding to transient stall flow regimes, the correlated TKE fields remain centered on the shear layer. As the angle of attack increases and the flow transitions into deep stall, a clear local maximum is seen at the TE normal to the chord as well as the in close proximity to the TE for both aerofoil geometries. The maximum magnitude of the TKE compared to the correlated TKE varies slightly depending on the case at $\tilde{k}_{max}/k_{max} \approx 0.25$.

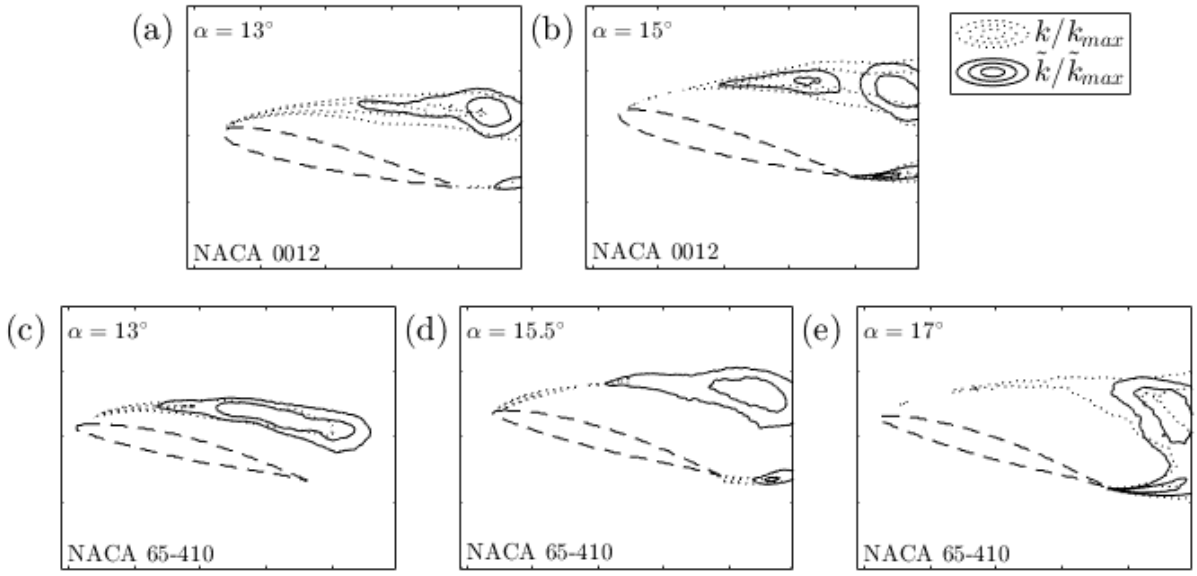

Fig 5: Turbulent kinetic energy (TKE) contours k/k_{max} (dotted) and TKE contours of flow correlated with dipole far field noise via sLSE (solid) for the NACA 0012 cases (a,b) and NACA 65-410 cases (c,d,e). The contour levels are taken at 50% and 75% for both quantities, highlighting the most intense regions.

6. Discussion

The use of time-resolved planar particle image velocimetry to reconstruct the instantaneous pressure fields focusing on separated symmetric and cambered aerofoils at $Re_c = 7.1 \times 10^4$ has been demonstrated. The unsteady pressure computed from these fields were applied to a simplified form of Curle's analogy to estimate the far-field acoustic pressure fluctuations. Through application of spectral linear stochastic estimation, the spatial locations in the velocity fields with high correlation to the noise generation were elucidated.

The results of figure 5 may be considered the key findings of the present study. Upon interpreting these contours, it is important to note that the noise generation considered here is dipole in nature. In other words, the noise originates at the surface of the aerofoil. Therefore, the

structures identified in figure 5 are indeed interacting with the surface of the aerofoil. It is perhaps unsurprising then that the structures are concentrated close to the trailing edge, as the trailing edge is known to be highly efficient at scattering noise (Roger & Moreau 2010). For cases in transient stall ($\alpha = 13°$), and particularly for the NACA 65-410, the structures are further upstream compared to the cases at higher angles of attack. This suggests a predominance of shear layer flapping in this flow regime. As the angle of attack increases, the correlated region of TKE is centered downstream above the trailing edge as well as in the shear layer directly at the trailing edge. The regions even connect at $\alpha = 17°$, indicating that noise generation in deep stall originates from a combination of shear layer and trailing edge structures. Together, the present results lend support to the picture proposed by Lacagnina *et al.* (2019) that the far-field noise is generated primarily by hydrodynamic interactions at the trailing edge.

7. References

- Brooks, T. F., Pope, D. S., & Marcolini, M. A. (1989). *Airfoil self-noise and prediction* (Vol. 1218). Washington, DC: National Aeronautics and Space Administration, Office of Management, Scientific and Technical Information Division.
- Curle, N. (1955). The influence of solid boundaries upon aerodynamic sound. *Proceedings of the Royal Society of London. Series A. Mathematical and Physical Sciences*, *231* (1187), 505-514.
- De Kat, R & Van Oudheusden, BW 2012 Instantaneous planar pressure determination from piv in turbulent flow. *Experiments in fluids* 52 (5), 1089–1106.
- Jakobsen, ML, Dewhirst, TP & Greated, CA 1997 Particle image velocimetry for predictions of acceleration fields and force within fluid flows. *Measurement Science and Technology* 8 (12), 1502
- Koschatzky, V., Moore, P. D., Westerweel, J., Scarano, F., & Boersma, B. J. (2011). High speed PIV applied to aerodynamic noise investigation. *Experiments in fluids*, *50*(4), 863-876.
- Koschatzky, V., Westerweel, J., & Boersma, B. J. (2011). A study on the application of two different acoustic analogies to experimental PIV data. *Physics of Fluids*, *23*(6), 065112.
- Lacagnina, G., Chaitanya, P., Berk, T., Kim, J. H., Joseph, P., Ganapathisubramani, B., ... & Pinelli, A. (2019). Mechanisms of airfoil noise near stall conditions. *Physical Review Fluids*, *4*(12), 123902.
- Laratro, A., Arjomandi, M., Kelso, R., & Cazzolato, B. (2014). A discussion of wind turbine interaction and stall contributions to wind farm noise. *Journal of Wind Engineering and Industrial Aerodynamics*, *127*, 1-10.
- Larsson, J., Davidson, L., Olsson, M., & Eriksson, L. E. (2004). Aeroacoustic investigation of an open cavity at low Mach number. *AIAA journal*, *42* (12), 2462-2473.

- Laskari, Angeliki, de Kat, Roeland & Ganapathisubramani, Bharathram 2016 Full-field pressure from snapshot and time-resolved volumetric piv. *Experiments in fluids* 57 (3), 44
- Lin, Zhouchen, Chen, Minming & Ma, Yi 2010 The augmented lagrange multiplier method for exact recovery of corrupted low-rank matrices. *arXiv preprint arXiv:1009.5055* .
- Mayer, Y. D., Zang, B., & Azarpeyvand, M. (2020). Aeroacoustic investigation of an oscillating airfoil in the pre-and post-stall regime. *Aerospace Science and Technology*, *103*, 105880.
- Moreau, S., Roger, M., & Christophe, J. (2009). Flow features and self-noise of airfoils near stall or in stall. In *15th AIAA/CEAS Aeroacoustics Conference (30th AIAA Aeroacoustics Conference)* (p. 3198).
- Podvin, Bérengère, Nguimatsia, Sylvain, Foucaut, Jean-Marc, Cuvier, Christophe & Fraigneau, Yann 2018 On combining linear stochastic estimation and proper orthogonal decomposition for flow reconstruction. *Experiments in Fluids* 59 (3), 1–12.
- Raffel, M, Willert, CE, Scarano, F, Kähler, CJ, Wereley, ST & Kompenhans, J 2018 Particle image velocimetry: A practical guide, third edit
- Roger, M., & Moreau, S. (2010). Extensions and limitations of analytical airfoil broadband noise models. *International Journal of Aeroacoustics*, *9*(3), 273-305.
- Scherl, Isabel, Strom, Benjamin, Shang, Jessica K, Williams, Owen, Polagye, Brian L & Brunton, Steven L 2020 Robust principal component analysis for modal decomposition of corrupt fluid flows. *Physical Review Fluids* 5 (5), 054401
- Sirovich, Lawrence 1987 Turbulence and the dynamics of coherent structures. iii. dynamics and scaling. *Quarterly of Applied mathematics* 45 (3), 583–590
- Sobral, Andrews, Bouwmans, Thierry & Zahzah, El-hadi 2016 Lrslibrary: Low-rank and sparse tools for background modeling and subtraction in videos. *Robust Low-Rank and Sparse Matrix Decomposition: Applications in Image and Video Processing*
- Taira, Kunihiko, Brunton, Steven L, Dawson, Scott TM, Rowley, Clarence W, Colonius, Tim, McKeon, Beverley J, Schmidt, Oliver T, Gordeyev, Stanislav, Theofilis, Vassilios & Ukeiley, Lawrence S 2017 Modal analysis of fluid flows: An overview. *AIAA Journal* 55 (12), 4013–4041.
- Tinney, C. E., Coiffet, F., Delville, J., Hall, A. M., Jordan, P., & Glauser, M. N. (2006). On spectral linear stochastic estimation. *Experiments in fluids*, *41*(5), 763-775.
- Turner, J. M., & Kim, J. W. (2020). Aerofoil dipole noise due to flow separation and stall at a low Reynolds number. *International Journal of Heat and Fluid Flow*, *86*, 108715.
- Van Gent, P. L., Michaelis, D., Van Oudheusden, B. W., Weiss, P. É., de Kat, R., Laskari, A., ... & Schrijer, F. F. J. (2017). Comparative assessment of pressure field reconstructions from

particle image velocimetry measurements and Lagrangian particle tracking. *Experiments in Fluids*, *58*(4), 33.

- Zang, B., Mayer, Y. D., & Azarpeyvand, M. (2021). Experimental Investigation of Near-Field Aeroacoustic Characteristics of a Pre-and Post-Stall NACA 65-410 Airfoil. *Journal of Aerospace Engineering*, *34*(6), 04021080.